Article

Enhanced Surface Properties of TiO$_2$-Based Coatings via Stevia-Assisted Spark Suppression: Insights from Density Functional Theory Calculations

Mosab Kaseem [1,*] , Ananda Repycha Safira [1] and Arash Fattah-alhosseini [2,*]

1 Corrosion and Electrochemistry Laboratory, Department of Nanotechnology and Advanced Materials Engineering, Sejong University, Seoul 05006, Republic of Korea; arepychas29@gmail.com
2 Department of Materials Engineering, Faculty of Engineering, Bu-Ali Sina University, Hamedan 65178-38695, Iran
* Correspondence: mosabkaseem@sejong.ac.kr (M.K.); a.fattah@basu.ac.ir (A.F.-a.)

Abstract: This study investigates the enhancement of surface properties in TiO$_2$-based coatings on the Ti-6Al-4V alloy through micro-arc oxidation (MAO), employing stevia sugar as a novel additive. By incorporating stevia sugar into acetate–glycerophosphate–tetraethoxysilane solutions used in MAO treatment, the porous morphology of TiO$_2$-based oxide layers is regulated. The incorporation of stevia moderates plasma discharge intensity, facilitating the formation of a uniform silicon-rich structure characterized by reduced porosity and pore size. This effect is attributed to the interaction between stevia and tetraethyl orthosilicate (TEOS), which modifies the TEOS hydrolysis process, thereby enhancing structural uniformity and stability while concurrently reducing plasma discharge intensity. Additionally, theoretical calculations offer a valuable understanding of the reactivity and interactions of stevia, TEOS, and their complex during the MAO process, laying the groundwork for further research and optimization in this promising field.

Keywords: Ti alloy; MAO; stevia; adsorption; corrosion; DFT

1. Introduction

Titanium and its alloys are highly valued for their versatility and exceptional properties, making them crucial materials in industries ranging from biomedical and aerospace to food processing and petrochemicals [1]. These alloys, particularly Ti6Al4V, are highly esteemed for their appropriateness as implant materials in dental and orthopedic applications [2]. Their corrosion resistance hinges on the composition of a protective layer containing TiO$_2$ and Al$_2$O$_3$ oxides on their surfaces, effectively shielding the alloy from corrosive attack [3,4]. However, the presence of aggressive ions like chloride can compromise this protective layer, leading to a significant decrease in corrosion resistance and making these alloys highly susceptible to localized corrosion.

Researchers have increasingly utilized micro-arc oxidation (MAO) to fabricate inorganic coatings, aiming to enhance the corrosion resistance of metals and their alloys. This method, well known for its plasma-assisted oxidation technique, is utilized on various metallic and metallic alloy substrates [5–7]. The properties of the MAO coatings are impacted by myriad factors, ranging from intrinsic attributes like substrate and electrolyte composition to extrinsic variables such as oxidation duration, electrolyte temperature, and electrical parameters [8]. Among these factors, the chemical composition of the electrolytes significantly impacts the electrochemical characteristics of the oxide layers generated via MAO. Nevertheless, a prevalent challenge in the production of MAO coatings arises from the use of environmentally harmful or toxic additives such as fluoride, aluminate, 1,3,5,7-Tetraazaadamantane, and Quinolin-8-ol [9]. The challenge at hand is, thus, to innovate new

electrolyte systems that employ eco-friendly additives, paving the way for the creation of high-performance coatings.

Introducing stevia sugar as an eco-friendly surface modifier presents an innovative approach to forming protective coatings on metal surfaces, leveraging its corrosion-inhibiting properties derived from steviol glycosides [10,11]. This protective layer acts as a shield, defending metals against corrosive substances and reducing the rate at which corrosion occurs. The concept involves employing ST, a natural sugar substitute, as a plasma-softening agent to reduce the intensity of plasma sparks during MAO treatment in an electrolyte-containing tetraethyl orthosilicate (TEOS). By controlling plasma discharges during MAO, it becomes feasible to manage defect formation, resulting in uniformity, and less coating, characterized by high corrosion resistance. Additionally, employing density functional theory (DFT) will elucidate the mechanism behind the inorganic layer formation during the MAO of Ti alloys. To date, no studies have proposed the utilization of TEOS and ST for regulating plasma discharges in MAO. Consequently, this study examines the effects of MAO treatments on Ti alloy samples in electrolytes, both with and without the addition of ST. The resulting oxide layers were analyzed for morphology, composition, and corrosion behavior. Additionally, the adsorption behavior of ST during the coating formation was investigated using DFT.

2. Materials and Methods

2.1. MAO Process

Ti-6Al-4V alloy disks were utilized as substrates for the MAO treatment. The preparation process involved initially polishing the samples with emery papers up to 2000 grade, followed by a thorough cleaning with distilled water and drying with a dryer. Two types of electrolytes were prepared as indicated in Table 1. The base electrolyte consisted of calcium glycerophosphate hydrate (CAGP) with the formula $C_3H_7CaO_6P.xH_2O$, calcium acetate monohydrate (CaAC) with the formula $Ca(CH_3CO_2)_2 \cdot H_2O$, and tetraethyl orthosilicate (TEOS) with the formula $SiC_8H_{20}O_4$. The other electrolyte had the same composition but included the addition of ST. The samples underwent oxidation through MAO for 3 min, employing a current density of 100 mA/cm^2. The sample coated in an electrolyte without ST was labeled 0ST, while the one with ST was labeled 10ST.

Table 1. Chemical compositions of the electrolytes used for the fabrication of the oxide layers.

Electrolyte	Composition				Conductivity ms/cm
	CaAC (M)	CaGly (M)	TEOS (mL)	ST (g)	
0ST	0.15	0.02	10	0	18.5
10ST	0.15	0.02	10	10	18.1

2.2. Characterization

Plasma sparks and voltage–time curves were recorded via Canon EOS700D during the coating process to investigate the influence of additives on the formation of the coating. The morphological characteristics of 0ST and 10ST samples were observed using a field emission electron microscope (FE-SEM, HITACHI SU8010, Hitachi, Tokyo, Japan) linked with an energy-dispersive X-ray spectrometer (EDS). Roughness measurements were carried out via atomic force microscopy (AFM, ToscaTM Analysis, Anton Paar, Graz, Austria) to assess the surface topography. The AFM was used to capture fine-scale surface features across the coating samples. The calculated roughness values (R_a) were derived from an average of 15 individual measurements taken at different locations on the samples. Additionally, the thickness of the MAO coatings was measured using an eddy-current meter tester (Minitest 2100, Electrophysik, Cologne, Germany). The analysis of porosity levels and micropore sizes was performed using Image J software (version 1.47). An X-ray diffraction (XRD, RIGAKU, D-MAX 2500, Tokyo, Japan) analysis was performed to understand the composition of complex materials fabricated on the surface by shining X-rays onto the sample in the angular range of 5–80° for crystal structure elucidation. Furthermore, samples were ascertained

through X-ray photoelectron spectroscopy (XPS, VG Microtech, ESCA 2000, VG Microtech, London, UK) providing data about different oxidation states of an element of the topmost layers. The electrochemical properties were assessed via potentiodynamic polarization (PDP) tests utilizing a three-electrode configuration immersed in a 3.5 wt.% NaCl solution. This setup included Ag/AgCl, a Pt plate, and the tested sample, serving as reference, counter, and working electrodes, respectively. The potential range during PDP tests was set at -250 mV to $+400$ mV with a scan rate of 1 mV/s, and the open-circuit potential (OCP) was stabilized for 5 h before conducting the PDP tests.

2.3. DFT Calculations

The designed molecules of TEOS, ST, and its complex (TEOS + ST) were made using GaussView 6.0 software [12]. The calculation for the structure optimization was conducted with Gaussian 09W software [13]. Density functional theory (DFT) with hybrid functional theory, which is unrestricted a Becke, 3-parameter, Lee–Yang–Parr (B3LYP) function [14,15], was chosen as the computational method. A 6-311G** basis set was selected as suggested by Plumley et al. [16], where B3LYP/6-311G** is one of the best functional/basis set combinations for complex systems and requires economical calculation. The optimized structure, Mulliken charge, HOMO–LUMO region, molecular electrostatic potential (MEP), electron localized function (ELF), density of states (DOS), reduced gradient density (RDG), and its scattered plot were visualized. Other than GaussView 6.0, Multiwfn and VMD were also used for the visualization [17]. The binding energy ($E_{binding}$) of the complex compound (TEOS + ST) is calculated by the following equation:

$$E_{binding} = E_{TEOS+ST} - E_{TEOS} - E_{ST} \tag{1}$$

where $E_{TEOS+ST}$, E_{TEOS}, and E_{ST} are the energy optimization of TEOS + ST, TEOS, and ST as fragments. The models of the ST, TEOS, and TEOS + ST interacted with TiO_2 on both rutile and anatase phases and were visualized using Material Studio 2020. The TiO_2 structures were downloaded from crystallography open database numbers 9015662 (rutile) [18] and 7206075 (anatase) [19]. To prove the point regarding the quality of the surface coating, the energy calculation of the TEOS–ST complex on TiO_2 using the $Dmol^3$ program [20–22] and GGA–PBE (generalized gradient approximation scheme with Perdew–Burke–Ernzerhoff) function, double-sized numerical basis set plus d-functional (DND) basis set, and followed by the Tkatchenko and Scheffler (TS) custom method for DFT-D were utilized. The calculations used a direct inversion in the iterative subspace (DIIS), thermal smearing of 0.1 Ha, and a self-consistent field (SCF) tolerance of 10^{-6}. The adsorption energy (E_{ads}) of the compounds to the TiO_2 layer is calculated by the following equation:

$$E_{ads} = E_{Total} - E_{additives} - E_{TiO2} \tag{2}$$

where $Ea_{dditives}$ and E_{TiO2} are the energy of additive (TEOS + ST) and TiO_2 as fragments, and E_{Total} is the energy of both optimized together. The TiO_2 was placed close to the active sites of the additives as reported based on the MEP surface visualization.

3. Results and Discussion

3.1. Voltage–Time Curves

The voltage response plotted against coating time for both the 0ST and 10ST samples treated with MAO is shown in Figure 1. Based on the voltage–time curve, three stages of MAO were distinguished by observing the gradual increase in voltage. The initial stage (Stage I) demonstrated a rapid slope increase as a passive film developed on the substrate through conventional anodization, adhering to Ohm's law [23–25]. This film continued to grow until reaching the breakdown voltage, where the applied potential exceeded the dielectric breakdown threshold, initiating plasma discharges. As a result, the cell voltage increased steadily due to the consistent growth rate of the oxide layer. Stage II was marked by a decreasing slope after breakdown voltage, while Stage III showed a further

decrease in slope, exhibiting plateau-like characteristics as the oxide layer growth rate remained relatively constant. From Figure 1a, it was observed that the breakdown voltage of the 10ST sample (~150.78 V) was lower compared to that of the 0ST sample (~170.50 V), despite minimal alterations in the electrolyte conductivity. These findings indicate that the physical and chemical adsorption of TEOS and ST on the bare substrate's surface during the initial stages of MAO might contribute to the differences in breakdown voltages observed between the 0ST and 10ST samples. Since the final voltages for both samples were nearly identical, around 321.81 V for the 0ST sample and approximately 310.16 V for the 10ST sample, it confirms that stevia molecules may only influence breakdown voltages by forming a complex with TEOS molecules (as further validated later). This complex is subsequently subjected to decomposition under the influence of plasma sparks beyond the breakdown voltage.
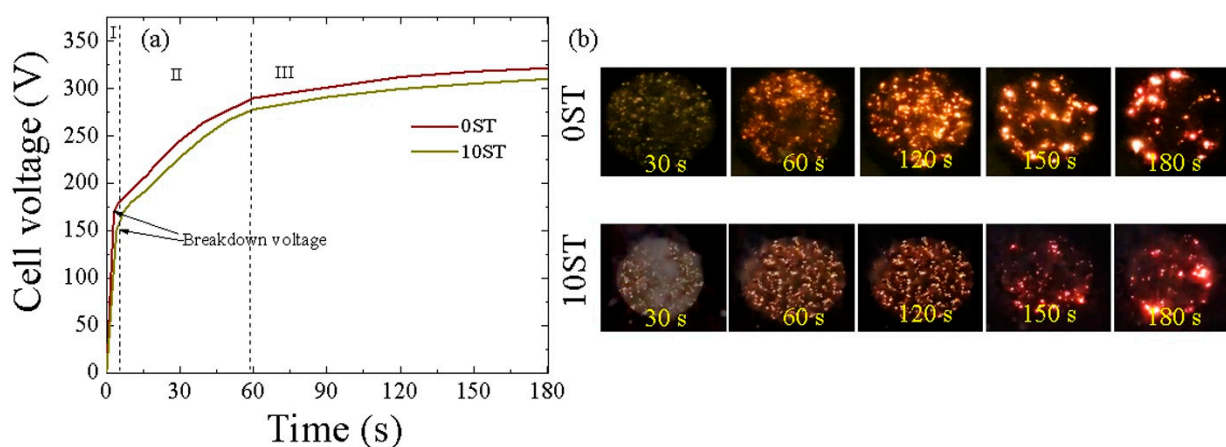

Figure 1. (**a**) Voltage–time curves of the 0ST and 10ST samples produced via MAO treatment of the Ti alloy; (**b**) The evolution of plasma discharges formed on the 0ST and 10ST samples during MAO over the coating durations of 30, 60, 120, 150, and 180 s.

Figure 1b depicts the images of plasma sparks observed during the MAO process of both the 0ST and 10ST samples. Overall, the plasma sparks tended to be weaker upon the addition of ST to the electrolyte. As illustrated in Figure 1b, without the ST additive, plasma discharges exhibited a non-uniform distribution, mainly concentrated in areas with high-intensity discharges. Conversely, the 10ST sample displayed a relatively more uniform and subdued intensity of discharges throughout all stages of the MAO process, suggesting the advantageous effect of stevia addition. The uniform and moderate sparks developed on the 10 ST sample were expected to lead to the generation of an oxide layer with fewer pores.

3.2. Morphologies of the Oxide Layers

Figure 2 illustrates surface morphologies, EDS elemental analyses, and AFM assessments of both the 0ST and 10ST samples. Despite differences in electrolyte composition, both samples exhibited the typical porous surface characteristic of MAO layers. The calculated pore size and porosity for the 0ST sample were approximately $7.18 \pm 1.51\%$ and 1.02 ± 0.7 μm, respectively, while for the 10ST sample, they were $4.32 \pm 0.84\%$ and 0.53 ± 0.24 μm, respectively. This implies that the presence of ST additive in the electrolyte led to a reduction in pore size and porosity, likely due to the generation of less energetic sparks upon its inclusion. As previously documented, denser coatings typically offer better corrosion protection than less compact ones. Therefore, it is reasonable to expect that the 10ST sample has better chemical stability than the 0ST sample.
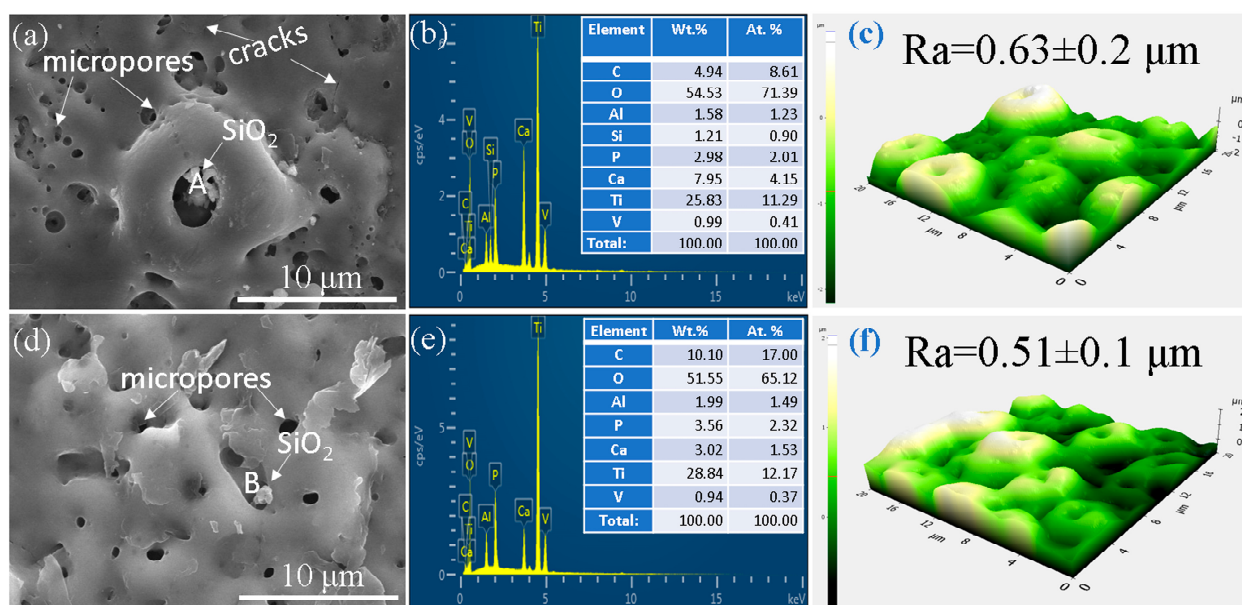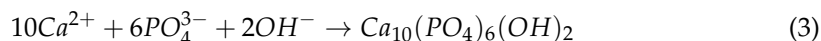
Figure 2. SEM images, EDS, and AFM results on the surface of the (**a**–**c**) 0ST sample and (**d**–**f**) 10ST sample.

The outcomes of the EDS analysis, as depicted in Figure 2b,e, uncovered the existence of the Ti, Al, and V elements originating from the substrate, alongside the Ca, P, O, and C elements derived from the electrolyte solution. The Ca/P ratio was approximately 2.67 for the 0ST sample and about 0.85 for the 10ST sample. These results emphasize the substantial effect of the ST additive on modifying the Ca/P ratio within the MAO coatings. In the 10ST sample, the oxide layer exhibits a Ca/P ratio below 1.67 in HA, whereas the 0ST sample demonstrates a Ca/P ratio exceeding 1.67, suggesting the addition of ST to the electrolyte would affect the electrochemical reactions that occur during the MAO. The deviation from the value of 1.67 in HA suggests that distinct chemical processes would occur during the MAO process in electrolytes both with and without the ST additive. The increased calcium content in the 0ST sample would be linked to the plasma-assisted hydrolysis of TEOS molecules. During the hydrolysis of TEOS, it liberates OH- ions into the electrolyte, aiding in the migration of Ca^{2+} cations towards the anode, thereby promoting their incorporation into the TiO_2 layer. Considering the calcium content in both 0ST and 10ST samples, it is hypothesized that the presence of ST would impede the hydrolysis of TEOS molecules, consequently decreasing the presence of Ca^{2+} cations in the 10ST sample. Figure 2c,f illustrate the surface roughness of the 0ST and 10ST samples, respectively. The R_a values for the oxide layer were slightly higher in the 0ST sample (~0.63 µm) compared to the 10ST sample (~0.51 µm), as revealed via AFM analysis capturing fine-scale surface features focusing on micro- to nanoscale roughness. The presence of larger pores in the 0ST sample likely contributed to increased surface irregularities, leading to a slightly higher R_a measurement. On the other hand, the addition of ST had an insignificant impact on the thickness of the oxide layer, with both samples showing nearly identical values of 6.5 ± 1.1 µm.

3.3. Compositional Analysis

Figure 3a illustrates the XRD patterns of the 0ST and 10ST samples, predominantly composed of TiO_2 phases (rutile and anatase) along with HA. Carbon-based compounds were absent from the XRD patterns of both oxide layers, indicating that carbon is probably incorporated into the coating layer as either elemental carbon or amorphous compounds [26]. The presence of HA in both samples is likely due to plasma conditions

during the MAO process, which facilitate interactions between Ca^{2+} and PO_4^{3-} ions (Equation (3)) [27].

$$10Ca^{2+} + 6PO_4^{3-} + 2OH^- \rightarrow Ca_{10}(PO_4)_6(OH)_2 \tag{3}$$

In Figure 3b, the Ti2p spectrum reveals three discernible peaks at 457.01, 457.56, and 463.06 eV, indicative of metallic Ti and anatase and rutile (TiO_2) [28,29]. Figure 3c demonstrates the deconvolution of the P2p spectrum, displaying peaks around 131.63, 132.1, 132.73, and 137.67 eV, suggesting the existence of P-O and PO_4^{3-} anion in the HA structure [30]. The confirmation of SiO_2 in the coating is established through the decomposition of the Si2p spectrum in Figure 3d, which exhibits multiple peaks at 100.95, 101.76, 102.39, and 120.9 eV [31,32].
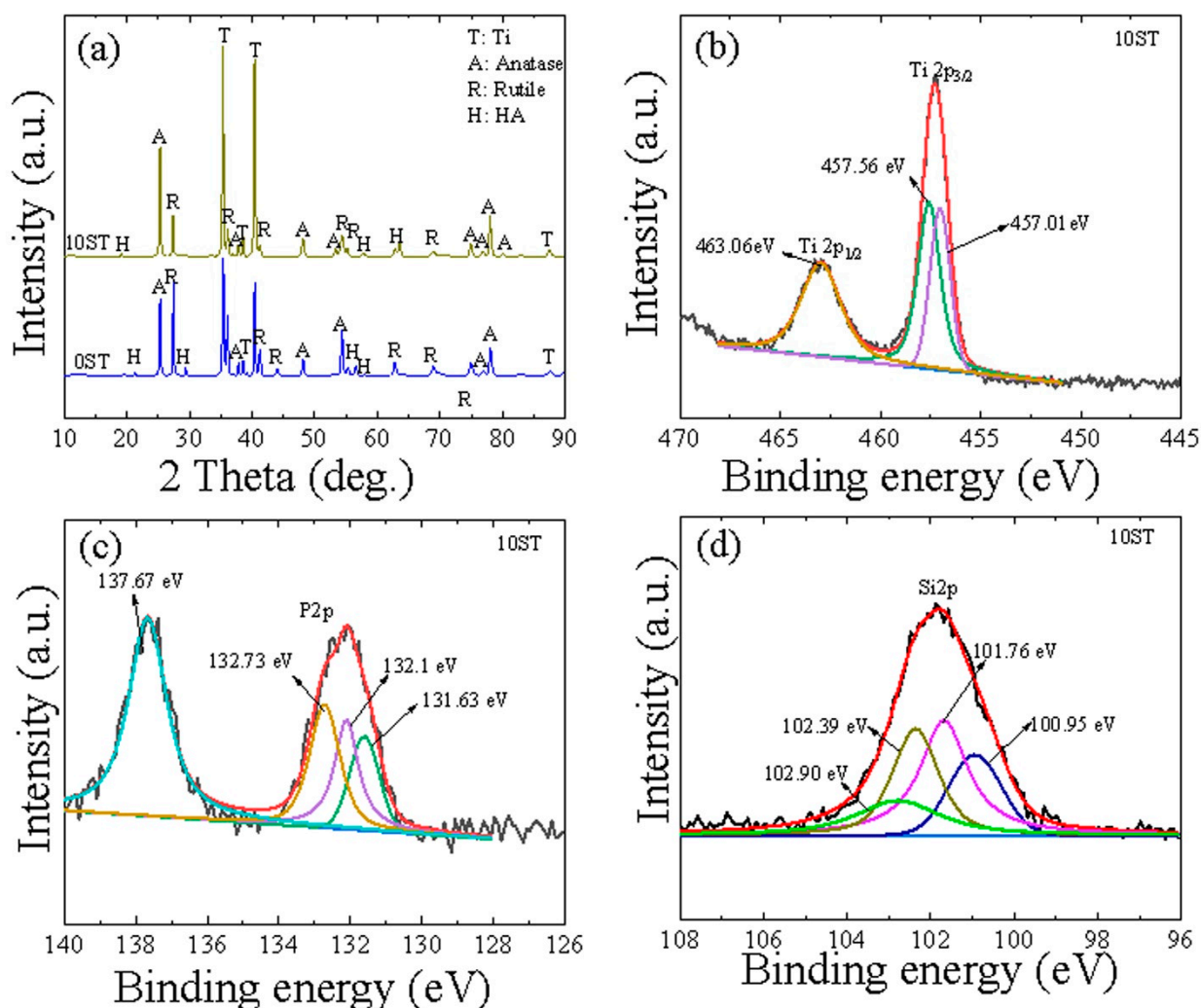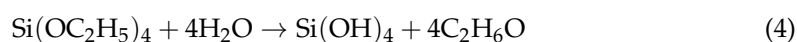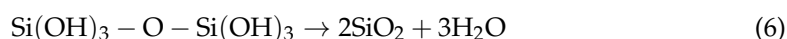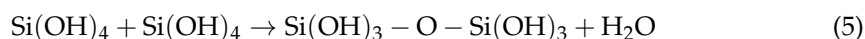

Figure 3. (**a**) XRD patterns of the 0ST and 10ST samples. (**b**–**d**) High-resolution XPS spectra of Ti2p, P2p, and Si2p, respectively, for the 10ST sample.

When examining the MAO process without ST additive, it is crucial to comprehend the reasons behind the robust spark occurrence in this scenario. The hydrolysis of TEOS initiates the breakdown of silicon–oxygen bonds within the molecule, leading to the formation of silanol groups (Si-OH) and ethyl alcohol as byproducts (Equation (4)). The subsequent condensation of these Si-OH groups leads to the creation of Si-O-Si bonds, facilitating the incorporation of SiO_2 in the amorphous form [33].

$$Si(OC_2H_5)_4 + 4H_2O \rightarrow Si(OH)_4 + 4C_2H_6O \tag{4}$$

$$Si(OH)_4 + Si(OH)_4 \rightarrow Si(OH)_3 - O - Si(OH)_3 + H_2O \tag{5}$$

$$Si(OH)_3 - O - Si(OH)_3 \rightarrow 2SiO_2 + 3H_2O \tag{6}$$

While the formation of a hybrid layer primarily composed of TiO_2 and SiO_2 is significant, it is essential to recognize that the hydrolysis of TEOS can produce byproducts that impede the electron avalanche [34]. The accumulation of these side products occurs on the surface of the barrier passive layer, which develops on the substrate surface before the breakdown phenomenon. The buildup of hydrolysis byproducts substantially hampers electron flow within the plasma, posing a hurdle to its continuous propagation. Consequently, the MAO process produces more intense plasma sparks when ST is absent. The increased spark intensity directly corresponds to the plasma's effort to penetrate the barriers formed by the buildup of hydrolysis products, thus surmounting the hindrance to electron flow. As a result, a coating with larger pores and a rough surface was developed in the 0ST sample. Conversely, the introduction of ST additive and its interaction with TEOS may form a complex that undergoes decomposition at the elevated temperature of MAO, thereby releasing new species that impact plasma discharges. Moreover, the addition of ST may potentially influence the hydrolysis of TEOS, thereby resulting in notable changes in the MAO process, particularly in terms of breakdown and final voltage values. Hence, the appearance of various moderate levels of spark intensity is probably due to an intricate interplay of factors, necessitating further exploration for comprehensive comprehension.

3.4. Corrosion Behavior

Figure 4 displays the PDP curves of the substrate, 0ST, and 10ST, after immersion in the test solution for 5 h. Parameters including corrosion potential (E_{corr}), corrosion current density (i_{corr}), and Tafel slopes (β_a/β_c) for both anodic and cathodic branches were determined via the Tafel approach. Additionally, the polarization resistance (R_p) values were calculated using Equation (7) [35].

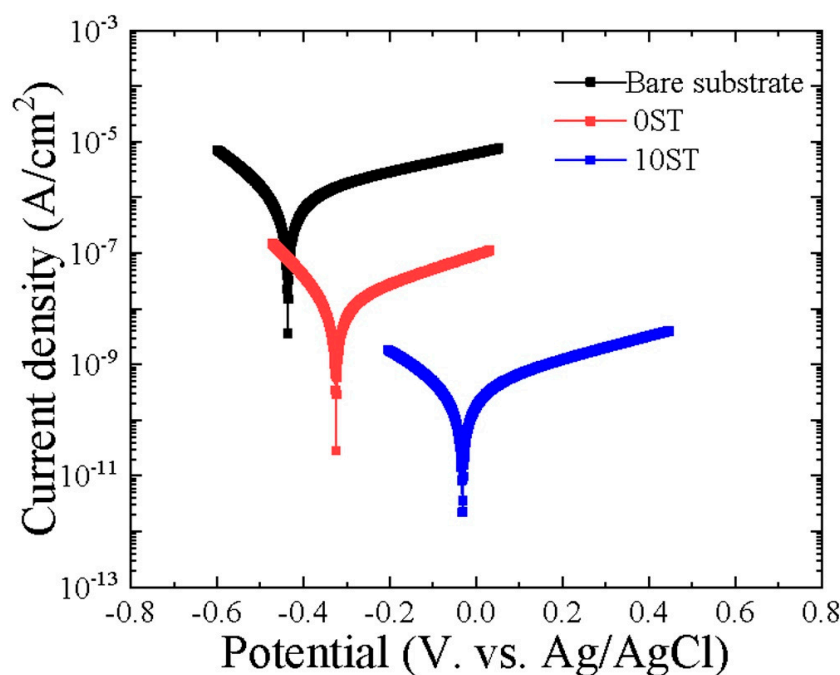$$R_p = \frac{\beta_a.\beta_c}{2.303\, i_{corr}(\beta_a + \beta_c)} \tag{7}$$

Figure 4. Potentiodynamic polarization curves of the bare substrate, 0ST, and 10ST samples, which were measured from -0.25 to 0.4 V vs. OCP.

The resulting data are tabulated in Table 2. The sample with higher E_{corr} and lower i_{corr} typically indicates better corrosion protection. As evident from Table 2, the addition of stevia to the electrolyte resulted in a shift of E_{corr} to higher values and i_{corr} to lower values, indicating an enhancement in the anticorrosive properties of the oxide layer. Specifically, the E_{corr} of the bare substrate shifted towards a nobler direction from −0.428 V to −0.022 V vs. Ag/AgCl after MAO treatment in an ST-containing solution, while its absence led to a shift in E_{corr} to −0.313 V vs. Ag/AgCl. Furthermore, the 10ST sample demonstrated the lowest i_{corr} value compared to the bare substrate and 0ST samples. Its measured value was four orders of magnitude less than that of the bare substrate and roughly one order lower than the 0ST sample. The enhancement in protective properties resulting from the addition of stevia to the electrolyte was evident in the significantly higher value of R_p, which was three orders of magnitude greater than that of the bare substrate and one order of magnitude higher than the 0ST sample. This suggests that samples treated in an electrolyte with ST provided better protection for the Ti-6Al-4V alloy substrate compared to the others. This improvement is likely due to the characteristics of the coating structure, including lower porosity and smaller pore size.

Table 2. Polarization results of the bare substrate, 0ST, and 10ST samples immersed in a 3.5 wt. % NaCl solution.

Sample	E_{corr} (V)	i_{corr} (A/cm^2)	β_a (V/Decade)	$\lvert \beta_c \rvert$ (V/Decade)	R_p (Ω.cm^2)
substrate	−0.428	1.01×10^{-6}	0.430	0.164	7.24×10^5
0ST	−0.313	8.77×10^{-9}	0.309	0.106	1.19×10^8
10ST	−0.022	1.72×10^{-10}	0.264	0.158	5.98×10^9

3.5. DFT Insights into Surface Adsorption and Reactivity

The chemical structures and optimized configurations of TEOS and TEOS + ST, along with their Mulliken charge analyses, are depicted in Figure 5, alongside corresponding results for ST molecules. The binding energy needed to form the complex of TEOS + ST is −30,000.24 eV, the negative value of the $E_{binding}$ indicates that bond formation is energetically favorable. In addition, changes in the Mulliken charges after the complex was shown where the charge of the Si atom became more positive (1.391 to 1.492 e) and the O atoms from both the carboxylic and hydroxyl groups became more negative (−0.568, −0.316, and −0.408 e to −0.342, −0.345, and −0.346). These changes happened due to the redistribution of electrons associated with the bonding or electron transfer process. To complement our understanding of the underlying interactions between TEOS, ST, and TEOS + ST and the MAO layer, Figures 6 and 7 are provided to offer a detailed view of the electronic and electrostatic properties of the TEOS and TES + ST complex. The highest occupied molecular orbital–lowest unoccupied molecular orbital (HOMO–LUMO) energy gap (ΔE) is a crucial indicator of chemical stability, where a wider energy gap signifies higher chemical stability, lower chemical reactivity, and greater kinetic stability [36]. Based on the ΔE values illustrated in Figure 6, the reactivity of the molecules followed the sequence TEOS < TEOS + ST < ST. TEOS exhibits a distinctive electronic characteristic with the most negative E_{HOMO} value, signifying a higher-energy barrier for electron donation, suggesting its reduced tendency to donate electrons. In contrast, ST alone displays a favorable electron-donating propensity, with the highest E_{HOMO} value, indicative of its capability to contribute electrons to surface interactions. In Figure 6a, the total density of states (TDOS) plot for TEOS reveals its highest peak at −13.4 eV, primarily stemming from contributions from carbon, hydrogen, oxygen, and silicon atoms within the compound. Si exhibits slight contributions at energy levels ranging from −21.1 to −18.2 eV, −14.6 to −11.3 eV, −10.0 to −6.6 eV, and 8.9 to 10.0 eV. The E_{HOMO} of TEOS is situated at −8.2 eV, with oxygen serving as the primary contributor at this energy level, followed by Si and C. This finding is further corroborated by the visualization of the HOMO region, which centers around the oxygen atom. In contrast, the E_{LUMO} at 7.9 eV is predominantly influenced by carbon and oxygen atoms, a conclusion

supported by the visualization of the LUMO region. As for ST, the TDOS plot shown in Figure 6b displays a more complex electronic structure with numerous detected peaks compared to TEOS. The highest peak in the electronic density occurs at −13.0 eV and is mainly attributed to contributions from carbon and hydrogen atoms within the compound. The electronic energy levels further reveal that ST's E_{HOMO} lies at −4.6 eV, centered around the C=C double bond in ST, as confirmed by the electronic density distribution. Additionally, the E_{LUMO} is situated at 0.7 eV and is primarily influenced by carbon and oxygen atoms, with the electron density distribution centered around the carboxyl functional group of ST. For comparison, Rouhani M. [37] calculated ST with the 6-311++G (d,p) basis set, resulting in 6.6 eV band gap energy, higher than the calculation in this study (5.3 eV). The difference lies in the additional diffuse functions (++G) that improve the description of electrons that are far from the nucleus, while this study uses a 6-311G (d,p) basis set without the diffuse functions. Despite lower accuracy, the 6-311G (d,p) basis set was chosen due to its lower cost of computational resources and faster calculation time considering the large number of atoms in the compound after the complexion with TEOS. Nevertheless, the optimized ST by Rouhani cannot be compared to TEOS and TEOS + ST in this paper, due to the difference in the basis set. The TEOS + ST complex, formed when TEOS and ST are added together into the electrolyte, exhibits distinct electronic properties as depicted in Figure 6c. The highest peak of the TDOS for the TEOS + ST complex is detected at an energy level of 3.5 eV, with carbon and oxygen atoms as the main contributors. The difference in the shape of the silicon peak (purple color) in Figure 6a,c may indicate interactions between the electronic states of different components after interaction with the ST compounds. Additionally, a broad silicon peak is detected across the energy levels from 1.3 to 10.0 eV. The E_{HOMO} for TEOS + ST is located at −6.7 eV, and carbon atoms primarily contribute to this peak. Interestingly, the HOMO region visualization reveals that it is centered not only around the C=C double bond but also around the cyclohexanol ring of ST. Furthermore, the E_{LUMO} at −0.7 eV is mainly contributed by C and O atoms, a finding that is confirmed by the LUMO region visualization which is centered around each carboxyl functional group. To elucidate the differences between the TEOS, ST, and TEOS + ST samples, the TDOS plots for the three molecules are illustrated in Figure 6d. A significant observation lies in the region where zero density of states (DOS) appears, which is an essential element of the DOS graph. The region of zero DOS of ST is located at −3.5 to −0.6 eV, while in TEOS's case, a large region of zero DOS is observed at −7.2 to 6.9 eV. The presence of this region indicates there are no available electronic states for electrons to occupy; therefore, the molecules with smaller regions of zero DOS will be more reactive. After the formation of the TEOS + ST complex, the presence of ST led to a smaller gap compared to TEOS alone, attributed to contributions from carbon and oxygen atoms. In addition, the changes in peak shapes and intensity especially at −15 to −5 and 0 to 10 eV may indicate interactions between the electronic states of different components (ST and TEOS). This variation raises the possibility of a shift in electronic properties for TEOS + ST, likely due to its more intricate molecular composition and larger molecular size, as compared to TE and ST samples.

　　The molecular electrostatic potential (MEP) maps presented in Figure 7a–c provide critical insights into the reactivity of TEOS, ST, and TEOS + ST. These MEP maps provide valuable guidance for understanding and predicting adsorption behavior during the MAO process. In TEOS, the presence of negative electrostatic regions surrounding oxygen atoms highlights their nucleophilic character, while the absence of positive electrostatic regions indicates limited electrophilic potential. Conversely, ST's MEP map showcases negative regions around oxygen atoms, particularly from the carboxyl and hydroxyl groups, indicating favorable electrophilic attack to these sites. Additionally, the presence of positive electrostatic regions around hydrogen atoms in the hydroxyl group suggests electrophilic reactivity. This result is consistent with the study of ST by Zhu et al. [38], although a different basis set was used (6–31 + G(d,p)). The main reactive sites are two oxygen and two hydrogen atoms as the electron donor and acceptor, respectively, from both the carboxyl and hydroxyl groups. In the case of TEOS + ST, the MEP map reveals an increase in

both positive and negative electrostatic regions, creating more active sites, and giving an advantage for intermolecular interaction. This combination suggests that TEOS + ST would be highly adsorbable due to its nucleophilic and electrophilic features.

Furthermore, for a more intuitive representation of lone-pair electrons, the electron localization function (ELF) based on localized molecular orbitals provides valuable insights [39]. In the case of TEOS molecules, as illustrated in Figure 7d, the ELF results reveal Si in yellow, indicating an intermediate to the high value of ELF. This suggests a high probability of finding electrons in this region, commonly associated with strong chemical bonds like covalent bonds and lone pairs of electrons. Additionally, in the ELF map of ST depicted in Figure 7e, the presence of a red region around the carbon atom signifies the presence of covalent bonds. Figure 7f further illustrates changes in ELF values, with Si transitioning from a blue to green color in the center, indicating a lower value of ELF compared to before the complex formation. These findings align with the Mulliken charge of 1.492 e, signifying that higher positive charges correspond to regions with less localized electrons.
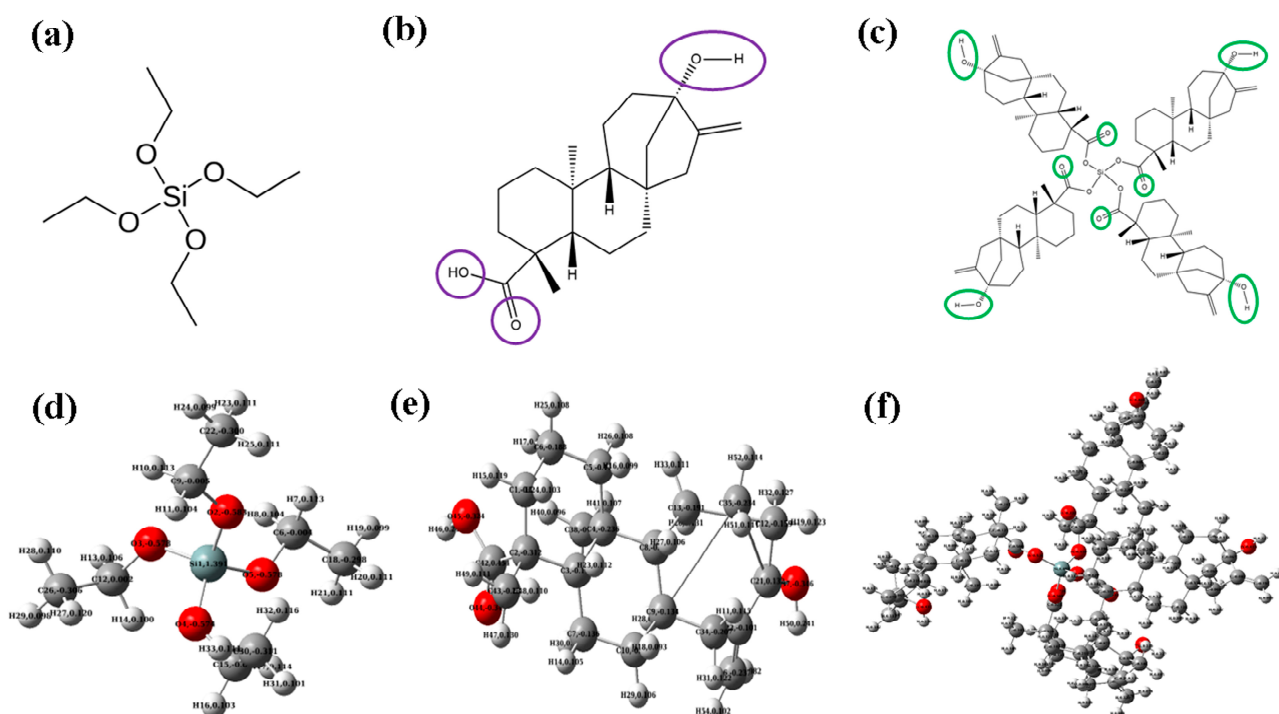

Figure 5. Two-dimensional structures and optimized structures with Mulliken atomic charge distribution of (**a**,**d**) TEOS, (**b**,**e**) ST, and (**c**,**f**) TEOS + ST. Purple circles represent the initial state with higher electron localization, while green circles indicate a decrease in electron localization after complex formation.

The study of weak interactions was investigated via RDG analysis, shown in Figure 7g–l, showing the ability of each molecule to interact through intermolecular interactions [40]. TEOS showed very little weak interaction while ST exhibited more interaction and more spikes at lower RDG levels; the hydrogen bonding is mainly formed by the hydroxyl and carboxyl groups of ST, resulting in a more functionalized network structure of ST on the substrate surface during the initial stages of the MAO process. After the complex, TEOS + ST shows the most interaction. However, as the molecule is larger, it shows a high steric effect. Moreover, the RDG scatter plot of ST shows more sharp and concentrated spikes than TEOS + ST, showing the TEOS + ST complex has a lower probability of being adsorbed on the substrate surface than ST. These intermolecular interactions such as H-bonding, π–π interactions, and electrostatic interaction formed synergistic effects and increased the strength of the coordination behavior of TEOS, ST, and TEOS + ST to construct a stable

protecting layer with a more favorable electron donor–acceptor character. Based on the preceding discussion, it can be inferred that the enhanced absorbability of the TEOS–ST complex on the bare substrate surface, compared to TEOS alone, likely contributes to the generation of lower-intensity plasma discharges, as shown in Figure 1. This, in turn, results in the formation of a less porous structure, as observed in the 10ST sample (Figure 2d), which exhibits higher corrosion resistance compared to the 0ST sample.
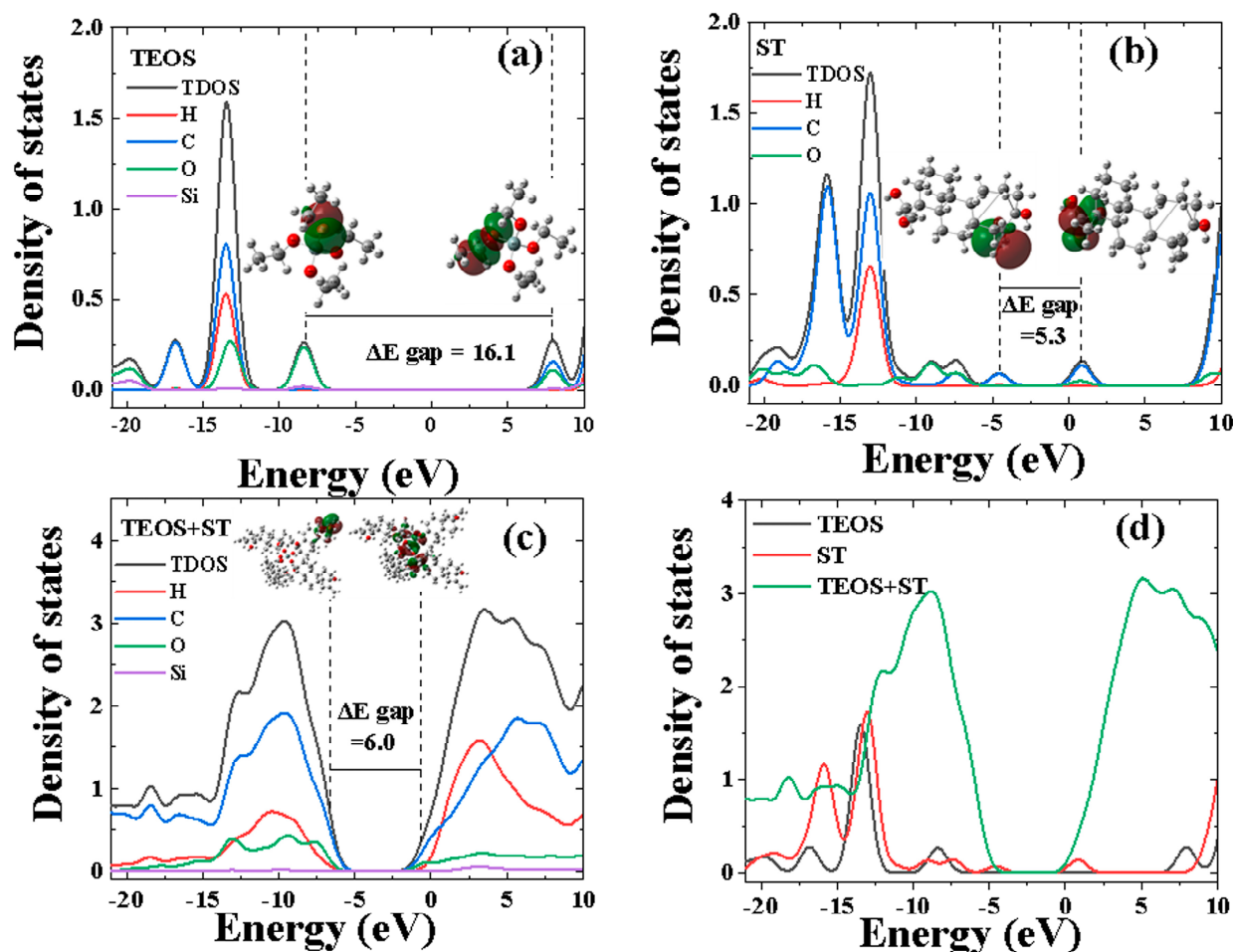

Figure 6. (**a**–**c**) HOMO–LUMO visualization and DOS fragment distribution for TEOS, ST, and TEOS + ST, respectively; (**d**) TDOS comparison of TEOS, ST, and TEOS + ST.

Chaudhary et al. [41] studied the adsorption and dissociation of TEOS on the rutile TiO_2 (110) surface with GGA–PAW (generalized gradient approximation-projector-augmented wave) method. For TEOS adsorption, one compound was placed on the slab, and C1s XPS spectra were simulated via the GPAW–PBE (grid-based projector-augmented wave) method. Varied energy adsorption ranging from 0.18 to 1.54 eV was obtained, depending on the bond dissociation [41]. It was reported that C-O or Si-O bond dissociation performs the highest E_{ads} of 1.54 eV, suggesting a high-stability configuration. Figure 8 depicts a visualization of ST, TEOS, and TEOS + ST on the rutile phase of TiO_2, showing the possibility of close-contact interaction (≤ 2.2 Å) between the compound with the surface. While ST and TEOS only show up to two possible interactions, TEOS + ST performs three possible interactions on the surface, marking the higher possibility of being adsorbed on the TiO_2. Other than the rutile phase, the anatase phase was also detected in the XPS results (Figure 3). Figure 9 shows the visualization of the studied compounds on the anatase phase, theoretically. The difference in shapes of this phase increases the potential of the compounds to interact with the surface. Each ST, TEOS, and TEOS + ST own five, six, and eight close interactions. Therefore, when the ST, TEOS, and TEOS + ST interacted

during the anatase phase, TiO$_2$ has a higher chance of undergoing a bond dissociation and performing better adsorption in the anatase phase of TiO$_2$ compared to the rutile phase. The E$_{ads}$ of TEOS + ST on the anatase phase of the TiO$_2$ surface (Ti$_{50}$O$_{84}$) was calculated to be 8.46 eV. However, this value cannot be compared to Chaudhary's results due to the difference in the functional and basis set used. To compare the adsorption energy of TEOS before and after the addition of ST, further research for the calculation of energy adsorption needs to be conducted.

Figure 7. MEP, ELF, RDG visualization, and plots of RDG vs. the electron density, respectively, for (**a**,**d**,**g**,**j**) TEOS, (**b**,**e**,**h**,**k**) ST, and (**c**,**f**,**i**,**l**) TEOS + ST.
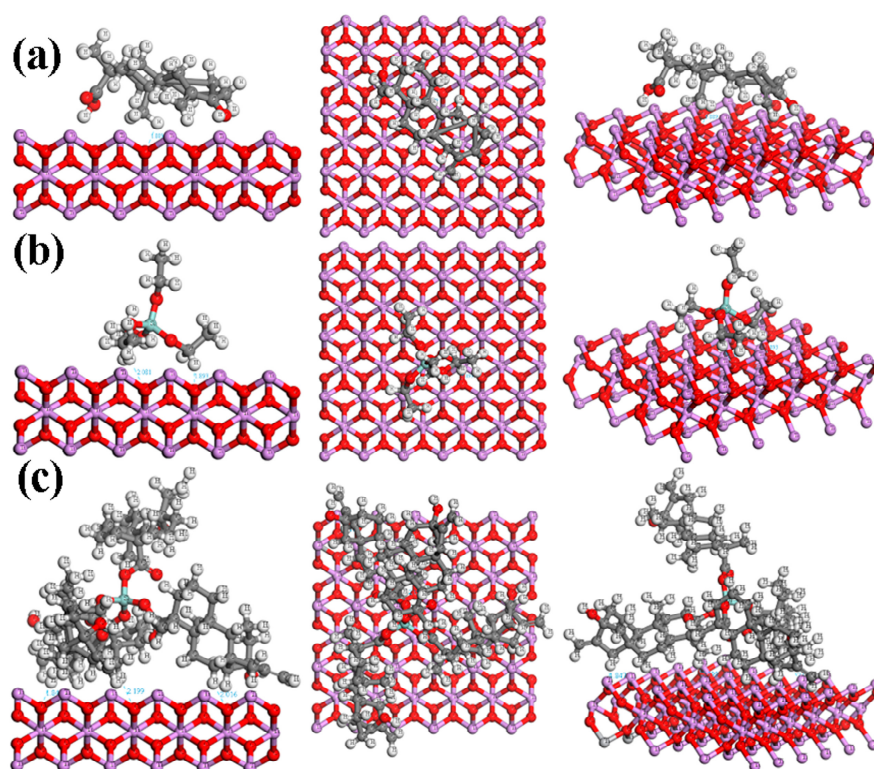
Figure 8. Top and side views of (**a**) ST, (**b**) TEOS, and (**c**) TEOS + ST interacted with the TiO_2 surface in the rutile phase.
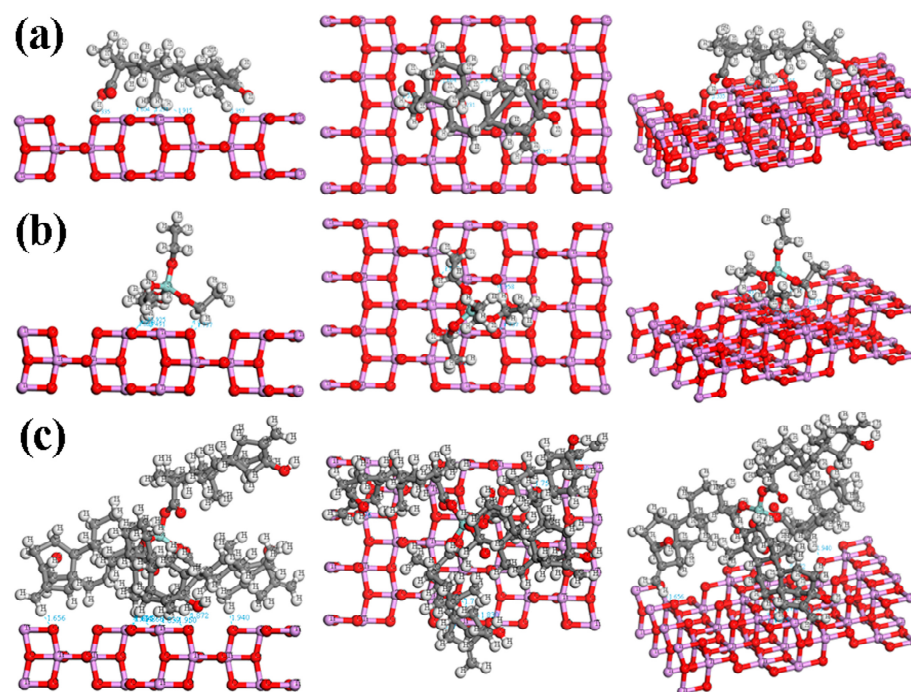
Figure 9. Top and side views of (**a**) ST, (**b**) TEOS, and (**c**) TEOS + ST interacted with the TiO_2 surface in the anatase phase.

4. Conclusions

This study demonstrates the effectiveness of incorporating stevia sugar as a novel additive during MAO coatings on the Ti-6Al-4V alloy. The inclusion of stevia sugar resulted in notable improvements in surface morphology and anticorrosive properties. Below are several key findings from this research.

1. The addition of stevia moderates the intensity of plasma discharge, which promotes the development of a uniform silicon-rich structure with decreased porosity and smaller pore size.
2. The sample treated in an electrolyte with stevia additive showed better corrosion resistance than the counterpart treated in an electrolyte without stevia.
3. The HOMO–LUMO energy gap analysis indicates that TEOS exhibits higher chemical stability, while ST shows a favorable electron-donating propensity.
4. The TDOS plots reveal distinct electronic structures, with TEOS + ST displaying unique characteristics. MEP maps highlight the electrophilic and nucleophilic reactivity of the molecules, suggesting their potential adsorption behavior.

These findings contribute significantly to our understanding of the underlying molecular mechanisms involved in the MAO process. Furthermore, they pave the way for future research aimed at enhancing protective coatings, especially those leveraging advantageous electron donor–acceptor properties.

References

1. Ozan, S.; Munir, K.; Biesiekierski, A.; Ipek, R.; Li, Y.; Wen, C. Titanium alloys, including nitinol. In *Biomaterials Science*; Elsevier: Amsterdam, The Netherlands, 2020; pp. 229–247.
2. Zhang, L.C.; Chen, L.Y.; Wang, L. Surface modification of titanium and titanium alloys: Technologies, developments, and future interests. *Adv. Eng. Mater.* **2020**, *22*, 1901258. [CrossRef]
3. Paghandeh, M.; Zarei-Hanzaki, A.; Abedi, H.; Vahidshad, Y.; Kawałko, J.; Dietrich, D.; Lampke, T. Compressive/tensile deformation behavior and the correlated microstructure evolution of Ti–6Al–4V titanium alloy at warm temperatures. *J. Mater. Res. Technol.* **2021**, *10*, 1291–1300. [CrossRef]
4. Nguyen, V.-T.; Cheng, T.-C.; Fang, T.-H.; Li, M.-H. The fabrication and characteristics of hydroxyapatite film grown on titanium alloy Ti-6Al-4V by anodic treatment. *J. Mater. Res. Technol.* **2020**, *9*, 4817–4825. [CrossRef]
5. Zehra, T.; Patil, S.A.; Shrestha, N.K.; Fattah-Alhosseini, A.; Kaseem, M. Anionic assisted incorporation of WO_3 nanoparticles for enhanced electrochemical properties of AZ31 Mg alloy coated via plasma electrolytic oxidation. *J. Alloys Compd.* **2022**, *916*, 165445. [CrossRef]
6. Roknian, M.; Fattah-Alhosseini, A.; Gashti, S.O. Plasma electrolytic oxidation coatings on pure Ti substrate: Effects of Na_3PO_4 concentration on morphology and corrosion behavior of coatings in ringer's physiological solution. *J. Mater. Eng. Perform.* **2018**, *27*, 1343–1351. [CrossRef]
7. Kaseem, M.; Choe, H.-C. Synchronized improvements in the protective and bioactive properties of plasma-electrolyzed layers via cellulose microcrystalline. *ACS Biomater. Sci. Eng.* **2023**, *9*, 197–210. [CrossRef]
8. Toorani, M.; Aliofkhazraei, M. Review of electrochemical properties of hybrid coating systems on Mg with plasma electrolytic oxidation process as pretreatment. *Surf. Interfaces* **2019**, *14*, 262–295. [CrossRef]
9. Kaseem, M.; Dikici, B. Optimization of surface properties of plasma electrolytic oxidation coating by organic additives: A review. *Coatings* **2021**, *11*, 374. [CrossRef]

10. Zhang, W.; Li, H.-J.; Liu, Y.; Wang, D.; Chen, L.; Xie, L.; Li, L.; Zhang, W.; Wu, Y.-C. Stevioside–Zn^{2+} system as an eco-friendly corrosion inhibitor for C1020 carbon steel in hydrochloric acid solution. *Colloids Surf. A Physicochem. Eng. Asp.* **2021**, *612*, 126010. [CrossRef]

11. Roy, A.; De, S. Extraction of steviol glycosides using novel cellulose acetate pthalate (CAP)—Polyacrylonitrile blend membranes. *J. Food Eng.* **2014**, *126*, 7–16. [CrossRef]

12. Dennington RD, I.I.; Keith, T.A.; Millam, J.M. *GaussView*, version 6.0. 16; Semichem Inc.: Shawnee Mission, KS, USA, 2016.

13. Frisch, M.J.; Trucks, G.W.; Schlegel, H.B.; Scuseria, G.E.; Robb, M.A.; Cheeseman, J.R.; Scalmani, G.; Barone, V.; Mennucci, B.; Petersson, G.A. *Gaussian 09*; Revision A.02; Gaussian Inc.: Wallingford, UK, 2009.

14. Becke, A.D. Density-functional thermochemistry. III. The role of exact exchange. *J. Chem. Phys.* **1993**, *98*, 5648–5652. [CrossRef]

15. Lee, C.; Yang, W.; Parr, R.G. Development of the Colle-Salvetti correlation-energy formula into a functional of the electron density. *Phys. Rev. B* **1988**, *37*, 785–789. [CrossRef] [PubMed]

16. Plumley, J.A.; Dannenberg, J.J. A comparison of the behavior of functional/basis set combinations for hydrogen-bonding in the water dimer with emphasis on basis set superposition error. *J. Comput. Chem.* **2011**, *32*, 1519–1527. [CrossRef] [PubMed]

17. Kaseem, M.; Min, J.H.; Ko, Y.G. Corrosion behavior of Al-1wt% Mg-0.85 wt% Si alloy coated by micro-arc oxidation using TiO$_2$ and Na$_2$MoO$_4$ additives: Role of Current density. *J. Alloys Compd.* **2017**, *723*, 448–455. [CrossRef]

18. Howard, C.J.; Sabine, T.M.; Dickson, F. Structural and thermal parameters for rutile and anatase. *Acta Crystallogr. Sect. B Struct. Sci.* **1991**, *47*, 462–468. [CrossRef]

19. Rezaee, M.; Khoie, S.M.M.; Liu, K.H. The role of brookite in mechanical activation of anatase-to-rutile transformation of nanocrystalline TiO$_2$: An XRD and Raman spectroscopy investigation. *CrystEngComm* **2011**, *13*, 5055–5061. [CrossRef]

20. Delley, B. From molecules to solids with the DMol3 approach. *J. Chem. Phys.* **2000**, *113*, 7756–7764. [CrossRef]

21. Delley, B. An all-electron numerical method for solving the local density functional for polyatomic molecules. *J. Chem. Phys.* **1990**, *92*, 508–517. [CrossRef]

22. *DMol^3*; Accelrys Inc.: San Diego, CA, USA, 2004.

23. Molaei, M.; Fattah-Alhosseini, A.; Nouri, M.; Mahmoodi, P.; Nourian, A. Incorporating TiO$_2$ nanoparticles to enhance corrosion resistance, cytocompatibility, and antibacterial properties of PEO ceramic coatings on titanium. *Ceram. Int.* **2022**, *48*, 21005–21024. [CrossRef]

24. Molaei, M.; Fattah-Alhosseini, A.; Nouri, M.; Mahmoodi, P.; Navard, S.H.; Nourian, A. Enhancing cytocompatibility, antibacterial activity and corrosion resistance of PEO coatings on titanium using incorporated ZrO$_2$ nanoparticles. *Surf. Interfaces* **2022**, *30*, 101967. [CrossRef]

25. Rogov, A.B.; Yerokhin, A.; Matthews, A. The role of cathodic current in plasma electrolytic oxidation of aluminum: Phenomenological concepts of the "soft sparking" mode. *Langmuir* **2017**, *33*, 11059–11069. [CrossRef] [PubMed]

26. Hussain, T.; Kaseem, M.; Ko, Y.G. Hard acid–hard base interactions responsible for densification of alumina layer for superior electrochemical performance. *Corros. Sci.* **2020**, *170*, 108663. [CrossRef]

27. Arun, S.; Ahn, S.-G.; Choe, H.-C. Surface characteristics of HA-coated and PEO-treated Ti-6Al-4V alloy in solution containing Ag nanoparticles. *Surf. Interfaces* **2023**, *39*, 102932. [CrossRef]

28. Marques Ida, S.; da Cruz, N.C.; Landers, R.; Yuan, J.C.; Mesquita, M.F.; Sukotjo, C.; Mathew, M.T.; Barão, V.A. Incorporation of Ca, P, and Si on bioactive coatings produced by plasma electrolytic oxidation: The role of electrolyte concentration and treatment duration. *Biointerphases* **2015**, *10*, 041002. [CrossRef] [PubMed]

29. Torres-Ceron, D.A.; Amaya-Roncancio, S.; Riva, J.S.; Vargas-Eudor, A.; Escobar-Rincon, D.; Restrepo-Parra, E. Incorporation of P^{5+} and P^{3-} from phosphate precursor in TiO$_2$:P coatings produced by PEO: XPS and DFT study. *Surf. Coat. Technol.* **2021**, *421*, 127437. [CrossRef]

30. Shokouhfar, M.; Dehghanian, C.; Montazeri, M.; Baradaran, A. Preparation of ceramic coating on Ti substrate by plasma electrolytic oxidation in different electrolytes and evaluation of its corrosion resistance: Part II. *Appl. Surf. Sci.* **2012**, *258*, 2416–2423. [CrossRef]

31. de Urquijo-Ventura, M.S.; Rao, M.S.; Meraz-Davila, S.; Torres-Ochoa, J.A.; Quevedo-Lopez, M.A.; Ramirez-Bon, R. PVP-SiO$_2$ and PVP-TiO$_2$ hybrid films for dielectric gate applications in CdS-based thin film transistors. *Polymer* **2020**, *191*, 122261. [CrossRef]

32. Eduok, U.; Faye, O.; Szpunar, J.; Khaled, M. Effect of silylating agents on the superhydrophobic and self-cleaning properties of siloxane/polydimethylsiloxane nanocomposite coatings on cellulosic fabric filters for oil–water separation. *RSC Adv.* **2021**, *11*, 9586. [CrossRef] [PubMed]

33. Diao, Z.; Shi, T.; Wang, S.; Huang, X.; Zhang, T.; Tang, Y.; Zhang, X.; Qiu, R. Silane-based coatings on pyrite for remediation of acid mine drainage. *Water Res.* **2013**, *47*, 4391–4402. [CrossRef]

34. Kaseem, M.; Zehra, T.; Khan, M.A.; Safira, A.R.; Cho, H.; Lee, J.; Lee, G.; Yang, H.W.; Park, N. Guar gum-driven high-energy plasma electrolytic oxidation for concurrent improvements in the electrochemical and catalytic properties of Ti-15 Zr alloy. *Surf. Interfaces* **2022**, *34*, 102403. [CrossRef]

35. Stern, M.; Geary, A.L. A theoretical analysis of the shape of polarization curves. *J. Electrochem. Soc.* **1957**, *104*, 56–63. [CrossRef]

36. Chaouiki, A.; Han, D.I.; Ko, Y.G. Multiwfn: A multifunctional wavefunction analyzer. *J. Colloid Interface Sci.* **2022**, *622*, 452–468. [CrossRef] [PubMed]

37. Rouhani, M. Full structural analysis of steviol: A DFT study. *J. Mol. Struct.* **2018**, *1173*, 679–689. [CrossRef]

38. Zhu, Y.; Ding, Y.; Tian, D.; Li, Y.; Zhuang, L.; Wang, Y.; Xiao, W.; Zhu, J. Theoretical design and preparation research of molecularly imprinted polymers for steviol glycosides. *J. Mol. Model.* **2021**, *27*, 1–12. [CrossRef] [PubMed]

39. Tüzün, B.; Bhawsar, J. Quantum chemical study of thiaozole derivatives as corrosion inhibitors based on density functional theory. *Arab. J. Chem.* **2021**, *14*, 102927. [CrossRef]

40. Johnson, E.R.; Keinan, S.; Mori-S'anchez, P.; Contreras-García, J.; Cohen, A.J.; Yang, W. Revealing noncovalent interactions. *J. Am. Chem. Soc.* **2010**, *132*, 6498–6506. [CrossRef]

41. Chaudhary, S.; Head, A.R.; Sánchez-De-Armas, R.; Tissot, H.; Olivieri, G.; Bournel, F.; Montelius, L.; Ye, L.; Rochet, F.; Gallet, J.-J.; et al. Real-time study of CVD growth of silicon oxide on rutile TiO_2 (110) using tetraethyl orthosilicate. *J. Phys. Chem. C* **2015**, *119*, 19149–19161. [CrossRef]